[1] Lelkov K.S *
[2] Chernomorsky A.I.

Cooperative Navigation for Ground and Aerial Robots

Journal of Electrical Systems

Abstract: - This study presents a novel approach to cooperative navigation for ground and aerial robots, utilizing sensor fusion techniques based on the Kalman filter. The primary objective is to enhance navigation accuracy by enabling real-time sharing and integration of positional information among robots. Through simulation results, we demonstrate that our method significantly improves the estimation of each robot's pose, effectively addressing the challenges posed by measurement noise and uncertainty. The results indicate that collaborative navigation not only optimizes individual robot performance but also enhances overall system resilience in complex environments.

Keywords: Robotics, Navigation, Sensor fusion, Kalman filter, Simulation, Cooperation.

I. INTRODUCTION

In recent years, the field of robotics has witnessed significant advancements, particularly in the development of autonomous systems capable of navigating complex environments [1]. Ground and aerial robots have emerged as critical components in various applications, ranging from search and rescue operations to environmental monitoring and agricultural management. As these robots become increasingly integrated into industrial processes, the need for effective cooperative navigation strategies has become paramount. Cooperative navigation refers to the ability of multiple robots - both ground-based and aerial - to work together to achieve a common objective while sharing information, resources, and spatial awareness.

The current state of research in cooperative navigation encompasses a variety of methodologies, including decentralized algorithms [2], multi-agent systems [3], and swarm intelligence [4]. Existing approaches have demonstrated promising results in enhancing the efficiency and robustness of navigation tasks. However, many studies tend to focus on either ground or aerial robots in isolation, with limited exploration of their synergistic capabilities when operating in tandem. This presents a significant gap in the literature, as ground and aerial robots possess complementary strengths that can be leveraged to improve navigation performance in challenging environments.

This research proposes a novel approach to cooperative navigation that integrates ground and aerial robots into a unified framework. By utilizing advanced communication protocols, real-time data sharing, and adaptive navigation algorithms, this approach aims to optimize navigation strategies across heterogeneous robot teams and enhance their situational awareness [5]. The novelty of this research lies in its emphasis on inter-robot collaboration, enabling ground robots to benefit from aerial reconnaissance and vice versa. This synergy not only improves navigation efficiency but also enhances the overall robustness of the robotic system in dynamic and unpredictable environments.

The primary goals of this research are threefold: first, to develop a comprehensive cooperative navigation framework that facilitates seamless interaction between ground and aerial robots; second, to validate this framework through simulation; and third, to analyze the performance improvements achieved through cooperation compared to traditional navigation methods. By addressing these objectives, this research aims to contribute valuable insights into the design and implementation of cooperative robotic systems.

The relevance of this work extends beyond theoretical contributions; it holds practical implications for numerous fields where cooperative navigation can enhance operational efficiency and safety. For instance, in disaster response scenarios, a coordinated team of ground and aerial robots can rapidly assess damage, locate survivors, and deliver supplies [6]. Similarly, in precision agriculture, such collaboration can optimize crop monitoring and resource allocation [7]. In modern airports, heterogeneous robot teams may be used for automatic aircraft inspections [8]. As industries increasingly seek automation solutions that are both effective and adaptable, this research aligns with the growing demand for innovative approaches to multi-robot coordination.

[1, 2] Department 305 of Moscow Aviation Institute, Moscow, Russia
* Corresponding Author Email: kon.lelkov@gmail.com

In this paper, we describe the application scenario for heterogeneous robots' team and the hardware setup. Then we develop navigation systems for ground and aerial robots based on the Kalman filter approach. Finally, we present the simulation results and discuss the benefits of cooperative navigation over the traditional navigation methods.

II. Application And Hardware

As was stated earlier - one of the novel applications for heterogeneous robots' teams is to conduct thorough inspections of parked aircraft for maintenance checks, damage assessment, and safety compliance. For this task the team composition usually includes few ground robots and one aerial robot. The ground robots are used to inspect the aircraft's fuselage, wings, landing gear, and other accessible components at close range. These robots can navigate around the aircraft, scanning for visible damage, leaks, or structural issues. The aerial robot is capable of flying around the aircraft to capture high-resolution images and videos from multiple angles. Drone can quickly cover larger areas and access hard-to-reach spots, such as the top of the wings or the tail section, providing a comprehensive overview of the aircraft's condition.

For simplicity, in this article we will consider a team of one ground robot and one aerial drone.

For the ground robot we picked an unmanned ground vehicle (UGV) with four drive wheels and the steering front wheel's axis [9]. This robot is equipped with the landing pad, allowing the unmanned aerial vehicle (UAV) to land on UGV in-between inspections for improved power management. The UGV's measurement systems include:

- magnetic encoders on each of the wheels, measuring their rotation rates $\dot{\phi}_1, \dot{\phi}_2, \dot{\phi}_3, \dot{\phi}_4$; as well as the optical sensor on the steering axis, measuring steering angle γ_g;
- inertial measurement unit (IMU), used mainly for measuring heading rotation rate $\dot{\psi}_g$;
- global navigation satellite system (GNSS) receiver, measuring global coordinates x_g, y_g and velocities $\dot{x}_g, \dot{y}_g$;
- LIDAR, mainly used for obstacle avoidance. Relative to the ground robot operating near the parked (static) aircraft, the LIDAR can be used to calculate robot's position and orientation relative to the aircraft [10];
- optical camera mounted on the landing pad upwards is used to detect UAV and calculate its pose relative to the UGV [11];
- stereo-camera mounted on the 2-axis gimbal is mainly used to inspect the aircraft's surface but can also be used to calculate robot's linear motion velocity relative to the aircraft [12].

For the aerial robot we consider a hex-rotor UAV [13]. Similarly, its measurement systems include:

- altitude sensor, measuring UAV's vertical coordinate z_a;
- IMU, used for measuring rotation rates $\omega_{ax}, \omega_{ay}, \omega_{az}$, and accelerations a_{ax}, a_{ay}, a_{az};
- GNSS receiver, measuring global coordinates x_g, y_g, z_g and velocities $\dot{x}_g, \dot{y}_g, \dot{z}_g$;
- optical camera mounted downwards is used to detect landing pad and calculate its position and orientation relative to the UAV;
- stereo-camera mounted on the 3-axis gimbal is mainly used to inspect the aircraft's surface but can also be used to calculate robot's linear motion velocity relative to the aircraft.

The described hardware setup and robot's compositions will serve as the basis for navigation systems development.

III. Navigation

The common approach to solving navigation problem for UGV and UAV is to use inertial-satellite sensor fusion [14, 15]. However, this approach may not be best suited for robots operating in close proximity of the aircraft since GNSS measurements become unreliable. To support the navigation solution and to increase its accuracy we propose three different ways to correct the navigation solution based on the relative information:

1. UGV can calculate its pose relative to the aircraft based on LIDAR measurements. Since the aircraft is parked – its pose in the global frame is known (to some extent, within margin of error). Hence, we can recalculate the relative position between UGV and the aircraft into global UGV's position.

2. UGV and UAV both can calculate their pose relative to each other based on the optical camera measurements. Considering that each robot has its own navigation system with global frame coordinates an output, this relative pose can be recalculated into global pose for both robots by taking into account the covariance of the opposing robot's navigation solution.
3. UGV and UAV both can calculate respective velocities relative to the aircraft's surface based on the stereo-camera measurements and photogrammetry methods. Since we have already established that the aircraft's position is known, these velocities can also be recalculated into the global frame.

All these methods rely on some form of computer vision algorithms to calculate robot's pose/velocity [16, 17, 18, 19]. These algorithms can be found in respective works and will not be described in this study.

Let us define three main coordinate frames used in this study (fig. 1).

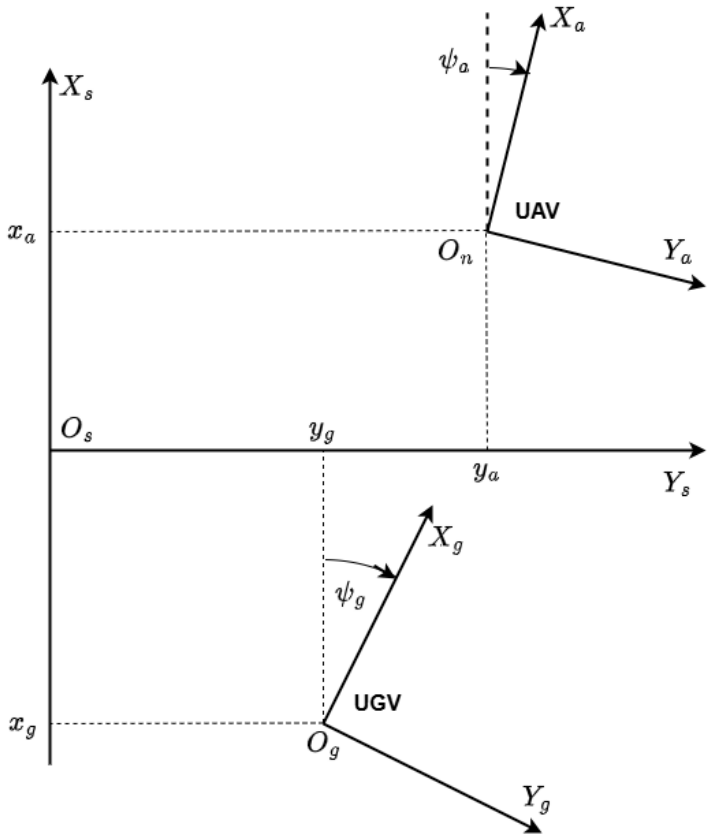

Fig. 1. Coordinate frames

The earth-fixed global frame $O_sX_sY_sZ_s$ (notation s denotes satellite measurements) is located at the setting starting point O_s. The UAV-fixed-frame $O_aX_aY_aZ_a$ is attached to the UAV's center of gravity. The UGV-fixed frame $O_gX_gY_gZ_g$ is respectively attached to the UGV's center of gravity. Orientation of all the frames follows the NED pattern [20]. Axis O_sX_s aligns with the north direction and axis O_sY_s points to the east. The remaining axis O_sZ_s points straight down, aligning with the gravity vector g. In the UAV-fixed-frame, O_aX_a is the longitudinal axis of the UAV and O_aY_a is the lateral one. Similarly, O_gX_g is the UGV's longitudinal axis and O_gY_g is the lateral axis of the ground robot.

Transformation between the coordinate frames is achieved by multiplying a vector with the corresponding direct cosine matrix. These matrices (considering NED pattern) can be found in most literature on aircraft dynamics. We will list here the matrices for transforming a vector from body frames $O_gX_gY_gZ_g$ and $O_aX_aY_aZ_a$ to the global frame $O_sX_sY_sZ_s$ for further reference:

$$\mathbf{R}_a^s = \begin{bmatrix} \cos\psi_a \cos\theta_a & \cos\psi_a \sin\theta_a \sin\gamma_a - \sin\psi_a \cos\gamma_a & \cos\psi_a \sin\theta_a \cos\gamma_a + \sin\psi_a \sin\gamma_a \\ \sin\psi_a \cos\theta_a & \sin\psi_a \sin\theta_a \sin\gamma_a + \cos\psi_a \cos\gamma_a & \sin\psi_a \sin\theta_a \cos\gamma_a - \cos\psi_a \sin\gamma_a \\ -\sin\theta_a & \cos\theta_a \sin\gamma_a & \cos\theta_a \cos\gamma_a \end{bmatrix};$$
$$\mathbf{R}_g^s = \begin{bmatrix} \cos\psi_g & -\sin\psi_g & 0 \\ \sin\psi_g & \cos\psi_g & 0 \\ 0 & 0 & 1 \end{bmatrix}, \quad (1)$$

where $\psi_a, \theta_a, \gamma_a$ are respectively heading, pitch and roll UAV angles; ψ_g - UGV's heading angle.

The reverse rotation can be achieved by multiplying a vector by transposed matrices respectively.

The core of navigation systems for UGV and UAV is based on applying Kalman filter approach to sensor fusion [21]. In general, discrete form the system's dynamic and measurements equations take is as follows:

$$\mathbf{X}' = \mathbf{F} \times \mathbf{X} + \mathbf{w};$$
$$\mathbf{Z} = \mathbf{H} \times \mathbf{X} + \mathbf{v}, \quad (2)$$

where $\mathbf{X}$ is the state vector of variables; $\mathbf{F}$ is the system' dynamic matrix; $\mathbf{w}$ - system noise vector; $\mathbf{Z}$ is the measurements vector; $\mathbf{H}$ is the measurements matrix and $\mathbf{v}$ is the measurements noise vector.

In order to apply Kalman filter for the proposed scenario, we need to define vectors $\mathbf{X}, \mathbf{Z}, \mathbf{w}, \mathbf{v}$ and matrices $\mathbf{F}, \mathbf{H}$ for both robots based on their motion and measurements models.

3.1 UGV navigation system

The state vector $\mathbf{X}^g$ for the UGV contains its coordinates x_g, y_g heading angle ψ_g, linear velocities $\dot{x}_g, \dot{y}_g$, heading rotation rate $\dot{\psi}_g$ and gyro bias $\Delta\omega_{gz}$:

$$\mathbf{X}^g = \begin{bmatrix} x_g & y_g & \psi_g & \dot{x}_g & \dot{y}_g & \dot{\psi}_g & \Delta\omega_{gz} \end{bmatrix}^T \quad (3)$$

The system dynamic matrix $\mathbf{F}^g$ can be obtained based on simple differential equations:

$$\mathbf{F}^g = \begin{bmatrix} 1 & 0 & 0 & dt & 0 & 0 & 0 \\ 0 & 1 & 0 & 0 & dt & 0 & 0 \\ 0 & 0 & 1 & 0 & 0 & dt & 0 \\ 0 & 0 & 0 & 1 & 0 & 0 & 0 \\ 0 & 0 & 0 & 0 & 1 & 0 & 0 \\ 0 & 0 & 0 & 0 & 0 & 1 & 0 \\ 0 & 0 & 0 & 0 & 0 & 0 & 1 \end{bmatrix}, \quad (4)$$

where dt is the integration step.

Since the UGV's measurement systems provide measurements with different frequencies, the navigation system should dynamically adjust measurement vector $\mathbf{Z}^g$ and matrix $\mathbf{H}^g$ based on the information available at each moment. We will define measurement submodels for each of the measurement systems and the full measurement equation (2) can then be constructed by concatenating the respective submodels [22].

The odometry system's measurements submodel can be derived from the kinematic motion equations for UGV [23]:

$$\dot{x}_g^{odo} = \frac{1}{4}\left(\dot{\phi}_1^{odo} r\cos\left(\gamma_1^{odo}\right) + \dot{\phi}_2^{odo} r\cos\left(\gamma_2^{odo}\right) + \dot{\phi}_3^{odo} r + \dot{\phi}_4^{odo} r\right);$$
$$\dot{y}_g^{odo} = \frac{1}{4}\left(\dot{\phi}_1^{odo} r\sin\left(\gamma_1^{odo}\right) + \dot{\phi}_2^{odo} r\sin\left(\gamma_2^{odo}\right)\right);$$
$$\dot{\psi}_g^{odo} = \frac{\dot{x}_g^{odo}}{l_f + l_r}\tan\left(\frac{\gamma_1^{odo} + \gamma_2^{odo}}{2}\right). \quad (5)$$

where $\dot{x}_g^{odo}, \dot{y}_g^{odo}, \dot{\psi}_g^{odo}$ are velocities and rotation rate of UGV, calculated based on odometry measurements; $\dot{\phi}_1^{odo}, \dot{\phi}_2^{odo}, \dot{\phi}_3^{odo}, \dot{\phi}_4^{odo}$ - UGV wheels' rotation rates measured by encoders; $\gamma_1^{odo}, \gamma_2^{odo}$ - steering angles of the UGV's front wheels; l_f, l_r - distances from UGV's center of gravity to the front and rear wheels' axes respectively; r is the radius of the wheels.

Odometry measurements submodel is as follows:

$$\mathbf{Z}^{odo} = \left[\dot{x}_g^{odo}, \dot{y}_g^{odo}, \dot{\psi}_g^{odo}\right]^T,$$
$$\mathbf{H}^{odo} = \begin{bmatrix} 0 & 0 & 0 & 1 & 0 & 0 & 0 \\ 0 & 0 & 0 & 0 & 1 & 0 & 0 \\ 0 & 0 & 0 & 0 & 0 & 1 & 0 \end{bmatrix},$$
$$\mathbf{v}^{odo} = \left[\sigma_{vel}^{odo}, \sigma_{vel}^{odo}, \sigma_{rate}^{odo}\right]^T, \quad (6)$$

where $\sigma_{vel}^{odo}, \sigma_{vel}^{odo}, \sigma_{rate}^{odo}$ are the zero-mean white noise signals with standard deviations of the respective odometry measurements.

Considering that IMU is mounted close to the UGV's center of gravity, its measurement submodel takes from:

$$\mathbf{Z}^{imu} = \left[\dot{\psi}_g^{imu}\right];$$
$$\mathbf{H}^{imu} = \begin{bmatrix} 0 & 0 & 0 & 0 & 0 & 1 & 1 \end{bmatrix};$$
$$\mathbf{v}^{imu} = \left[\sigma_{gyr}^{imu}\right], \quad (7)$$

where $\dot{\psi}_g^{imu}$ is the UGV's heading angular rate measured by IMU and σ_{gyr}^{imu} is the zero-mean white noise signal with standard deviation of the gyroscope measurements.

The GNSS receiver provides measurements for its antenna location. Let's assume that the antenna is displaced by l_{gx} and l_{gy} from the center of gravity:

$$x_g^{gnss} = x_g + l_{gx}\cos\psi_g - l_{gy}\sin\psi_g;$$
$$y_g^{gnss} = y_g + l_{gx}\sin\psi_g + l_{gy}\cos\psi_g;$$
$$\dot{x}_g^{gnss} = \dot{x}_g + \dot{\psi}_g l_{gx}\cos\psi_g - \dot{\psi}_g l_{gy}\sin\psi_g;$$
$$\dot{y}_g^{gnss} = \dot{y}_g + \dot{\psi}_g l_{gx}\sin\psi_g + \dot{\psi}_g l_{gy}\cos\psi_g, \quad (8)$$

where $x_g^{gnss}, y_g^{gnss}, \dot{x}_g^{gnss}, \dot{y}_g^{gnss}$ are the coordinates and velocities measured by GNSS receiver.

Based on the equations (8), the GNSS measurement submodel is as follows:

$$\mathbf{Z}^{gnss}=\begin{bmatrix} x_g^{gnss}-l_{gx}\cos\psi_g+l_{gy}\sin\psi_g \\ y_g^{gnss}-l_{gx}\sin\psi_g-l_{gy}\cos\psi_g \\ \dot{x}_g^{gnss} \\ \dot{y}_g^{gnss} \end{bmatrix};$$

$$\mathbf{H}^{gnss}=\begin{bmatrix} 1 & 0 & 0 & 0 & 0 & 0 & 0 \\ 0 & 1 & 0 & 0 & 0 & 0 & 0 \\ 0 & 0 & 0 & 1 & 0 & l_{gx}\cos\psi_g-l_{gy}\sin\psi_g & 0 \\ 0 & 0 & 0 & 0 & 1 & l_{gx}\sin\psi_g+l_{gy}\cos\psi_g & 0 \end{bmatrix};$$

$$\mathbf{v}^{gnss}=\left[\sigma_{pos}^{gnss},\sigma_{pos}^{gnss},\sigma_{vel}^{gnss},\sigma_{vel}^{gnss}\right]^T, \tag{9}$$

where $\sigma_{pos}^{gnss},\sigma_{vel}^{gnss}$ are the zero-mean white noise signals with standard deviations of the respective GNSS measurements.

UGV pose calculated based on the LIDAR measurements can be described as:

$$\mathbf{Z}^{lidar}=\left[x_g^{lidar},y_g^{lidar},\psi_g^{lidar}\right]^T;$$

$$\mathbf{H}^{lidar}=\begin{bmatrix} 1 & 0 & 0 & 0 & 0 & 0 & 0 \\ 0 & 1 & 0 & 0 & 0 & 0 & 0 \\ 0 & 0 & 1 & 0 & 0 & 0 & 0 \end{bmatrix};$$

$$\mathbf{v}^{lidar}=\left[\sigma_{pos}^{lidar},\sigma_{pos}^{lidar},\sigma_{ang}^{lidar}\right]^T, \tag{10}$$

where $x_g^{lidar},y_g^{lidar},\psi_g^{lidar}$ are the coordinates and the heading angle calculated based on LIDAR measurements and $\sigma_{pos}^{lidar},\sigma_{ang}^{lidar}$ arethe zero-mean white noise signals with standard deviations of the respective lidar measurements.

Optical camera measurements submodel is as follows:

$$\mathbf{Z}^{opt}=\left[x_g^{opt},y_g^{opt},\psi_g^{opt}\right]^T;$$

$$\mathbf{H}^{opt}=\begin{bmatrix} 1 & 0 & 0 & 0 & 0 & 0 & 0 \\ 0 & 1 & 0 & 0 & 0 & 0 & 0 \\ 0 & 0 & 1 & 0 & 0 & 0 & 0 \end{bmatrix};$$

$$\mathbf{v}^{opt}=\left[\sigma_{pos}^{opt},\sigma_{pos}^{opt},\sigma_{ang}^{opt}\right]^T, \tag{11}$$

where $x_g^{opt},y_g^{opt},\psi_g^{opt}$ are the coordinates and the heading angle calculated based on optical camera measurements and $\sigma_{pos}^{opt},\sigma_{ang}^{opt}$ arethe zero-mean white noise signals with standard deviations of the respective measurements.

Stereo-camera (photogrammetry) submodel takes form:

$$\mathbf{Z}^{stereo}=\left[\dot{x}_g^{stereo},\dot{y}_g^{stereo}\right]^T;$$

$$\mathbf{H}^{stereo}=\begin{bmatrix} 0 & 0 & 0 & 1 & 0 & 0 & 0 \\ 0 & 0 & 0 & 0 & 1 & 0 & 0 \end{bmatrix};$$

$$\mathbf{v}^{stereo}=\left[\sigma_{vel}^{stereo},\sigma_{vel}^{stereo}\right]^T, \tag{12}$$

where $\dot{x}_g^{stereo}, \dot{y}_g^{stereo}$ are the UGV's velocities calculated based on stereo-camera measurements and σ_{vel}^{stereo} arethe zero-mean white noise signals with standard deviations of the respective measurements.

The estimates of the state vector's (3) elements, can be derived based on the relationships established in equations (4) through (12). This derivation will be achieved through the application of the Kalman filter algorithm [24]. The Kalman filter operates by integrating a series of measurements over time, accounting for both the inherent dynamics of the system and the statistical properties of the noise affecting the observations.

$$\begin{aligned}
&\mathbf{y} = \mathbf{Z} - \mathbf{HX};\\
&\mathbf{S} = \mathbf{HPH}^T + \mathbf{R};\\
&\mathbf{K} = \mathbf{PH}^T\mathbf{S}^{-1};\\
&\mathbf{X}_k = \mathbf{X}_{k-1} + \mathbf{Ky};\\
&\mathbf{P}_k = \left(\mathbf{I} - \mathbf{KH}\right)\mathbf{P}_{k-1},
\end{aligned} \tag{13}$$

where $\mathbf{y}$ – measurement residual vector; $\mathbf{S}$ – covariancematrix of measurement residuals; $\mathbf{R}$ – diagonalmatrixofmeasurementnoises; $\mathbf{K}$ – Kalman gain; $\mathbf{P}$ – state covariance matrix; $\mathbf{I}$ – identity matrix.

3.2 UAV navigation system

The approach for developing UAV's navigation system is generally the same as for UGW's one. First, we define state vector $\mathbf{X}^a$ as follows:

$$\mathbf{X}^a = \left[\mathbf{p}_{1x3}, \mathbf{s}_{1x3}, \mathbf{n}_{1x3}, \mathbf{q}_{1x3}, \mathbf{r}_{1x3}, \mathbf{u}_{1x3}, \mathbf{g}_{1x3}\right]^T \tag{14}$$

Thecomponentsof $\mathbf{X}^a$ arethefollowingrow-vectors: $\mathbf{p}_{1x3} = \left[x_{as}, y_{as}, z_{as}\right]$ – UAV'spositionvector; $\mathbf{s}_{1x3} = \left[\dot{x}_{as}, \dot{y}_{as}, \dot{z}_{as}\right]$ – UAV'svelocityvector; $\mathbf{n}_{1x3} = \left[\ddot{x}_{as}, \ddot{y}_{as}, \ddot{z}_{as}\right]$ – accelerationvectoroftheUAV; $\mathbf{q}_{1x3} = \left[\psi_a, \theta_a, \gamma_a\right]$ – UAV'sorientationvector; $\mathbf{r}_{1x3} = \left[\dot{\psi}_a, \dot{\theta}_a, \dot{\gamma}_a\right]$ – UAV'sangularratesvector; $\mathbf{u}_{1x3} = \left[a_{ax0}, a_{ay0}, a_{az0}\right]$ – UAV accelerometers' bias vector; $\mathbf{g}_{1x3} = \left[\omega_{x0}, \omega_{y0}, \omega_{z0}\right]$ – UAV gyroscopes' bias vector.

System dynamic matrix F^a can be obtained based on simple differential equations:

$$\mathbf{F}^a = \begin{bmatrix}
\mathbf{I}_{3x3} & dt\cdot\mathbf{I}_{3x3} & 0 & 0 & 0 & 0 & 0\\
0 & \mathbf{I}_{3x3} & dt\cdot\mathbf{I}_{3x3} & 0 & 0 & 0 & 0\\
0 & 0 & k_{ar}\cdot\mathbf{I}_{3x3} & 0 & 0 & 0 & 0\\
0 & 0 & 0 & \mathbf{I}_{3x3} & dt\cdot\mathbf{I}_{3x3} & 0 & 0\\
0 & 0 & 0 & 0 & k_{ad}\cdot\mathbf{I}_{3x3} & 0 & 0\\
0 & 0 & 0 & 0 & 0 & \mathbf{I}_{3x3} & 0\\
0 & 0 & 0 & 0 & 0 & 0 & \mathbf{I}_{3x3}
\end{bmatrix} \tag{15}$$

where k_a, k_d are the air resistance and damping coefficients respectively.

Just as we did for UGV, we will define measurement submodels for each of the UAV's measurement systems and the full measurement equation (2) can then be later constructed by concatenating the respective submodels.

Once again considering that IMU is mounted close to the UAV's center of gravity, the measured acceleration $a_{ax}^{imu}, a_{ay}^{imu}, a_{az}^{imu}$ and angular rate $\omega_{ax}^{imu}, \omega_{ay}^{imu}, \omega_{az}^{imu}$ values are as follows:

$$\begin{bmatrix} a_{ax}^{imu} - a_{ax0} \\ a_{ay}^{imu} - a_{ay0} \\ a_{az}^{imu} - a_{az0} \end{bmatrix} = \left(\mathbf{R}_a^s\right)^T \times \begin{bmatrix} \ddot{x}_{as} \\ \ddot{y}_{as} \\ \ddot{z}_{as} \end{bmatrix};$$

$$\omega_{ax}^{imu} = \dot{\gamma}_a - \dot{\psi}_a \sin\theta_a + \omega_{ax0};$$

$$\omega_{ay}^{imu} = \frac{\dot{\theta}_a + \dot{\psi}_a \cos\theta_a \tan\gamma_a}{\cos\gamma_a - \sin\theta_a \tan\gamma_a} + \omega_{ay0};$$

$$\omega_{az}^{imu} = \frac{\dot{\psi}_a \cos\theta_{at} - \dot{\theta}_a \tan\gamma_a}{\cos\gamma_a - \sin\theta_a \tan\gamma_a} + \omega_{az0}, \tag{16}$$

Based on the equations (16), IMU measurements submodel takes form:

$$\mathbf{Z}^{imu} = \left[\omega_{ax}^{imu}, \omega_{ax}^{imu}, \omega_{ax}^{imu}, a_{ax}^{imu}, a_{ax}^{imu}, a_{ax}^{imu}\right]^T;$$

$$\mathbf{H}^{imu} = \begin{bmatrix} 0 & 0 & 0 & 0 & \mathbf{h}_{g3x3} & 0 & \mathbf{I}_{3x3} \\ 0 & 0 & \left(\mathbf{R}_a^s\right)^T & 0 & 0 & \mathbf{I}_{3x3} & 0 \end{bmatrix};$$

$$\varpi^{imu} = \left[\sigma_{gyr}^{imu}, \sigma_{gyr}^{imu}, \sigma_{gyr}^{imu}, \sigma_{acc}^{imu}, \sigma_{acc}^{imu}, \sigma_{acc}^{imu}\right]^T;$$

$$\mathbf{h}_{g3x3} = \begin{bmatrix} -\sin\theta_a & 0 & 1 \\ \dfrac{\cos\theta_a \tan\gamma_a}{\cos\gamma_a - \sin\theta_a \tan\gamma_a} & \dfrac{1}{\cos\gamma_a - \sin\theta_a \tan\gamma_a} & 0 \\ \dfrac{\cos\theta_a}{\cos\gamma_a - \sin\theta_a \tan\gamma_a} & \dfrac{-\tan\gamma_a}{\cos\gamma_a - \sin\theta_a \tan\gamma_a} & 0 \end{bmatrix}, \tag{17}$$

where $\sigma_{gyr}^{imu}, \sigma_{gyr}^{imu}, \sigma_{gyr}^{imu}, \sigma_{acc}^{imu}, \sigma_{acc}^{imu}, \sigma_{acc}^{imu}$ are the zero-mean white noise signals with standard deviations of the IMU measurements.

The altitude sensor provides direct altitude measurements z_a^{baro}. The respective submodel is as follows:

$$\mathbf{Z}^{baro} = \left[z_a^{baro}\right];$$

$$\mathbf{H}^{baro} = \left[0,0,1,0,0,0,0,0,0,0,0,0,0,0,0,0,0,0,0,0,0,0\right];$$

$$\mathbf{v}^{baro} = \left[\sigma_{pos}^{baro}\right], \tag{18}$$

where σ_{pos}^{baro} isthe zero-mean white noise signal with standard deviations of the altitude sensor measurements.

The GNSS receiver measurement submodel is similar to (8)-(9), but let's assume that in this case the receiver's antenna is displaced from UAV's center of gravity only along $O_a Z_a$ axis by the distance l_{az}:

$$x_a^{gnss} = x_a + l_{az}\left(\cos\psi_a \sin\theta_a \cos\gamma_a + \sin\psi_a \sin\gamma_a\right);$$

$$y_a^{gnss} = y_a + l_{az}\left(\sin\psi_a \sin\theta_a \cos\gamma_a - \cos\psi_a \sin\gamma_a\right);$$

$$z_a^{gnss} = z_a + l_{az} \cos\theta_a \cos\gamma_a;$$

$$\dot{x}_a^{gnss} = \dot{x}_a + \dot{\theta}_a l_{az} \cos\psi_a \cos\theta_a - \dot{\gamma}_a l_{az}\left(\cos\psi_a \sin\theta_a \sin\gamma_a - \sin\psi_a \cos\gamma_a\right);$$

$$\dot{y}_a^{gnss} = \dot{y}_a + \dot{\theta}_a l_{az} \sin\psi_a \cos\theta_a - \dot{\gamma}_a l_{az}\left(\sin\psi_a \sin\theta_a \sin\gamma_a + \cos\psi_a \cos\gamma_a\right);$$

$$\dot{z}_a^{gnss} = \dot{z}_a, \tag{19}$$

where $x_a^{gnss}, y_a^{gnss}, z_a^{gnss}, \dot{x}_a^{gnss}, \dot{y}_a^{gnss}, \dot{z}_a^{gnss}$ are the values, measured by GNSS receiver.

Considering (19), the GNSS measurements submodel takes form:

$$\mathbf{Z}^{gnss} = \begin{bmatrix} x_a^{gnss} - l_{az}\left(\cos\psi_a \sin\theta_a \cos\gamma_a + \sin\psi_a \sin\gamma_a\right) \\ y_a^{gnss} - l_{az}\left(\sin\psi_a \sin\theta_a \cos\gamma_a - \cos\psi_a \sin\gamma_a\right) \\ z_a^{gnss} - l_{az}\cos\theta_a \cos\gamma_a \\ \dot{x}_a^{gnss} \\ \dot{y}_a^{gnss} \\ \dot{z}_a^{gnss} \end{bmatrix};$$

$$\mathbf{H}^{gnss} = \begin{bmatrix} \mathbf{I}_{3x3} & 0 & 0 & 0 & 0 & 0 & 0 \\ 0 & \mathbf{I}_{3x3} & 0 & 0 & \mathbf{h}_{s3x3} & 0 & 0 \end{bmatrix};$$

$$\mathbf{v}^{gnss} = \left[\sigma_{pos}^{gnss}, \sigma_{pos}^{gnss}, \sigma_{pos}^{gnss}, \sigma_{vel}^{gnss}, \sigma_{vel}^{gnss}, \sigma_{vel}^{gnss}\right]^T, \tag{20}$$

where $$\mathbf{h}_{s3x3} = \begin{bmatrix} 0 & l_{az}\cos\psi_a \cos\theta_a & -l_{az}\left(\cos\psi_a \sin\theta_a \sin\gamma_a - \sin\psi_a \cos\gamma_a\right) \\ 0 & l_{az}\sin\psi_a \cos\theta_a & -l_{az}\left(\sin\psi_a \sin\theta_a \sin\gamma_a + \cos\psi_a \cos\gamma_a\right) \\ 0 & 0 & 0 \end{bmatrix}.$$

Optical camera measurements submodel is similar to (11), but also contains the altitude:

$$\mathbf{Z}^{opt} = \left[x_a^{opt}, y_a^{opt}, z_a^{opt}, \psi_a^{opt}\right]^T;$$

$$\mathbf{H}^{opt} = \begin{bmatrix} \mathbf{I}_{3x3} & 0 & 0 & 0 & 0 & 0 & 0 \\ 0 & 0 & 0 & \mathbf{h}_{a3x3} & 0 & 0 & 0 \end{bmatrix};$$

$$\mathbf{h}_{a3x3} = \begin{bmatrix} 1 & 0 & 0 \\ 0 & 0 & 0 \\ 0 & 0 & 0 \end{bmatrix};$$

$$\mathbf{v}^{opt} = \left[\sigma_{pos}^{opt}, \sigma_{pos}^{opt}, \sigma_{pos}^{opt}, \sigma_{ang}^{opt}\right]^T, \tag{21}$$

where $x_a^{opt}, y_a^{opt}, z_a^{opt}, \psi_a^{opt}$ are the UAV's coordinates and the heading angle calculated based on optical camera measurements.

And, finally, stereo-camera measurement submodel is as follows:

$$\mathbf{Z}^{stereo} = \left[\dot{x}_a^{stereo}, \dot{y}_a^{stereo}, \dot{z}_a^{stereo}\right]^T;$$

$$\mathbf{H}^{stereo} = \begin{bmatrix} 0 & \mathbf{I}_{3x3} & 0 & 0 & 0 & 0 & 0 \end{bmatrix};$$

$$\mathbf{v}^{stereo} = \left[\sigma_{vel}^{stereo}, \sigma_{vel}^{stereo}, \sigma_{vel}^{stereo}\right]^T, \tag{22}$$

where $\dot{x}_a^{stereo}, \dot{y}_a^{stereo}, \dot{z}_a^{stereo}$ are the UAV's velocities calculated based on stereo-camera measurements.

The estimates of the state vector's (14) elements, can also be obtained through the application of the Kalman filter algorithm (13) based on the relationships established in equations (15) through (22).

IV. SIMULATION

In this section, simulation results are presented to evaluate the developed navigation systems. During the simulation the UGV and UAV move along respective given trajectories in vicinity of the A320 aircraft. The UGV performs the inspection of the bottom half of the aircraft's surface, while UAV inspects the upper half. Robot's motion trajectories overlap a few times to allow for navigation correction based on computer vision algorithms. For

simulation purposes we define optical camera correction conditions as follows: horizontal distance between two robots is less than 5 meters, the robots are in the direct line of sight of each other. We assume that the correction frequency for optical camera measurements is set to 5 Hz. The UGV's navigation correction is available most of the time (except the times when aircraft's landing gears are overshadowing each other) at 1 Hz frequency. The stereo-camera correction data is available when the robots are within 4 meters from the aircraft's surface at 2 Hz frequency (since photogrammetry algorithms are computationally expensive). The IMU, altitude sensor and encoders measurement frequencies are set to 100 Hz. The GNSS measurement frequency is set to 10 Hz. The rest of the simulation parameters are as follows:starting position: $(-2,0,0)$ m; white noise standard deviations - $\sigma_{vel}^{odo} = 0.4$ m/s ; $\sigma_{rate}^{odo} = 0.05$ 1/c ; $\sigma_{gyr}^{imu} = 0.01$ 1/s ; $\sigma_{acc}^{imu} = 0.015$ m/s^2 ; $\sigma_{pos}^{gnss} = 0.7$ m ; $\sigma_{vel}^{gnss} = 0.05$ m/s ; $\sigma_{pos}^{lidar} = 0.05$ m ; $\sigma_{ang}^{lidar} = 0.04$; $\sigma_{pos}^{opt} = 0.15$ m ; $\sigma_{ang}^{opt} = 0.06$; $\sigma_{vel}^{stereo} = 0.2$ m/s $\sigma_{pos}^{baro} = 0.25$ m.

The simulation results of cooperative UAV and UGV navigation are presented in fig. 2-6.

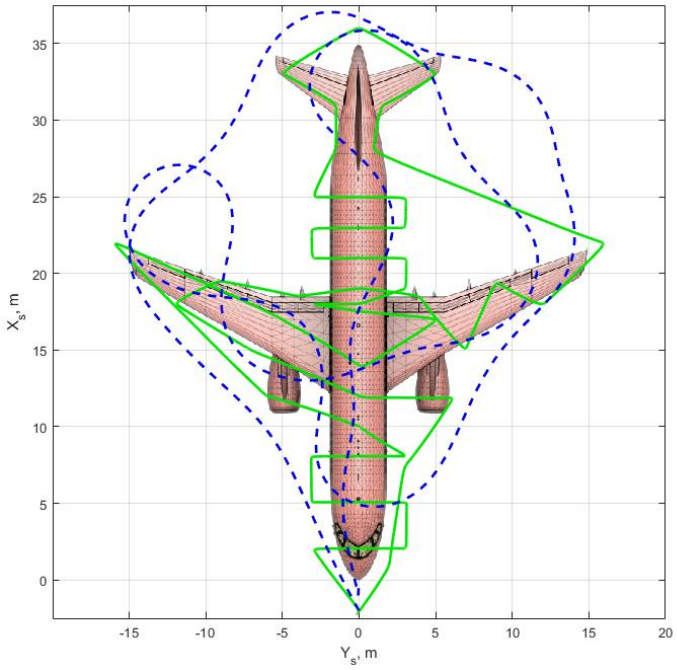

Fig. 2. Motion trajectories for UAV (green) and UGV (blue)

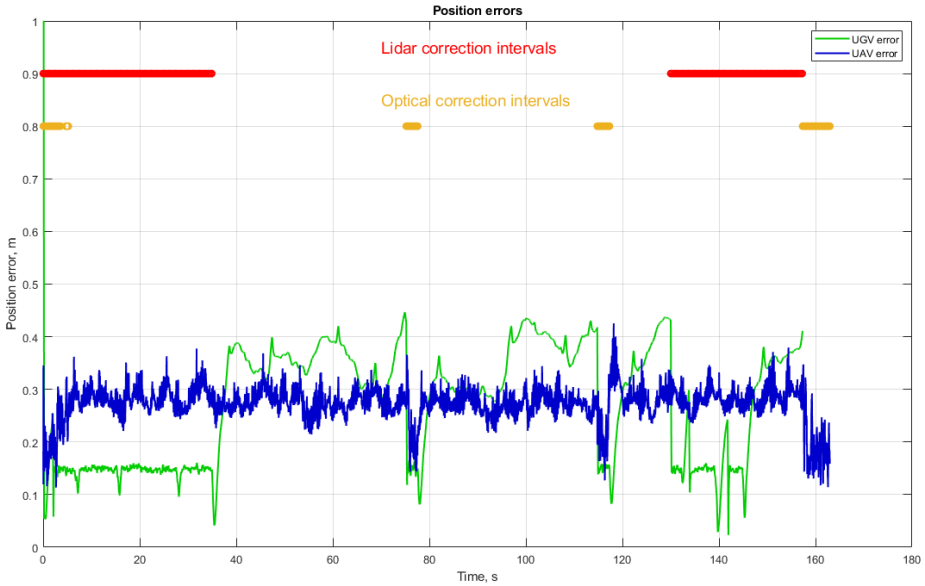

Fig. 3. UGV and UAV coordinates estimation errors

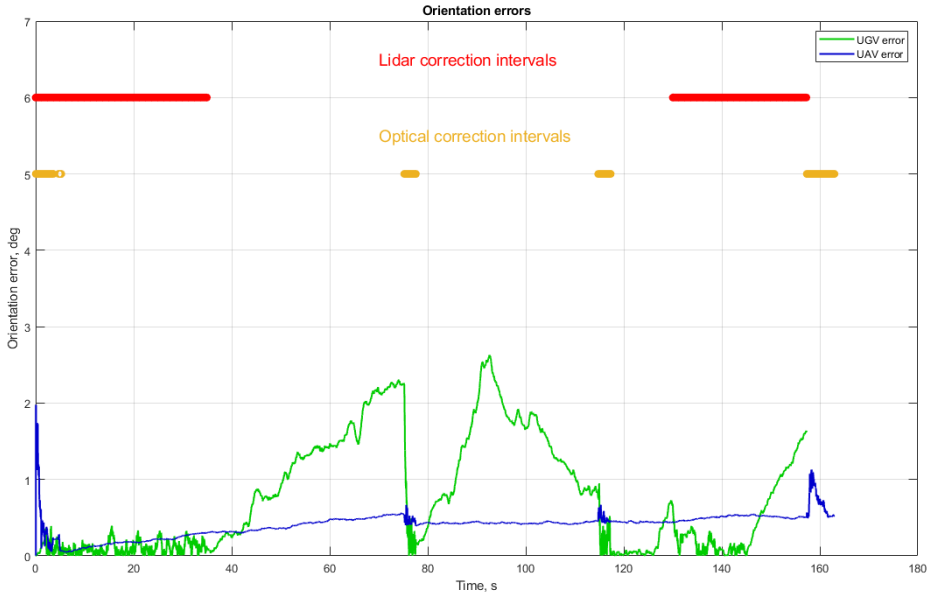

Fig. 4. UGV and UAV orientations estimation errors

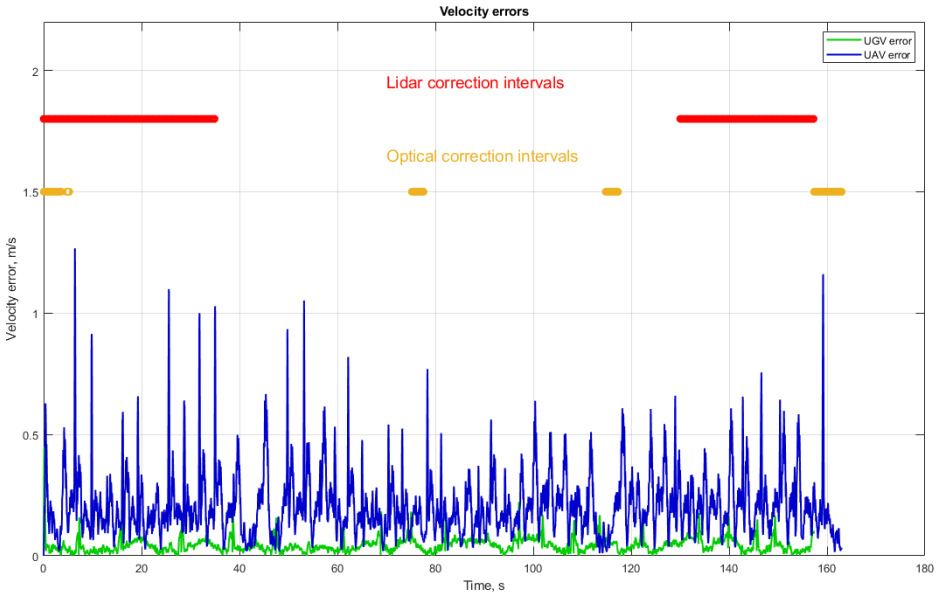

Fig. 5. UGV and UAV velocities estimation errors

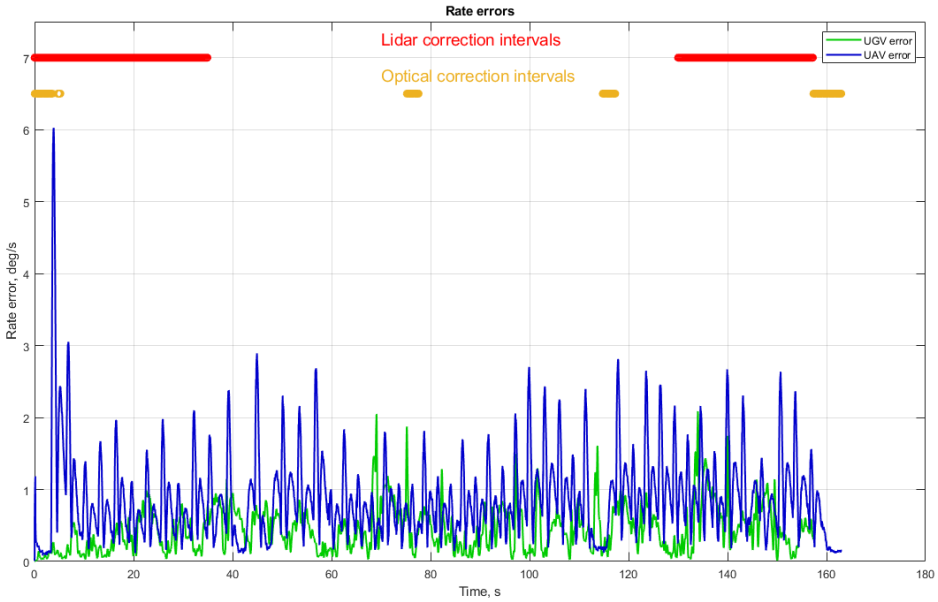

Fig. 6. UGV and UAV angular rates estimation errors

Fig. 3 shows that the mean position estimation errors are 0.27 m for UGV and 0.27 m for UAV. Standard deviation equals to 0.11 m and 0.04 m respectively. These results indicate a fairly high navigation accuracy. The obtained values are acceptable when implementing automatic aircraft inspection systems.

The orientation estimation errors presented in fig. 4 indicate that the mean orientation estimation errors are equal to 0.76 deg for UGV and 0.4 deg for UAV. In the same time, the standard deviation of these errors equals to 0.73 deg and 0.15 deg respectively.

Analysis of the results on figs 5,6 confirms that the proposed cooperative navigation approach allows for precise linear velocity and angular rate estimation. For UGV mean velocity error is 0.04 m/s and mean angular rate error equals to 0.45 deg/s. The respective standard deviations are: 0.03 m/s and 0.31 deg/s. For UAV mean errors are equal to 0.21 m/s and 0.89 deg/s with standard deviations of 0.13 m/s and 0.61 deg/s respectively.

For research integrity, we provide the simulation results for conventional navigation approaches in the same conditions (these results were achieved by disabling LIDAR, optical and stereo cameras correction channels). The results are partially presented on fig. 7-8.

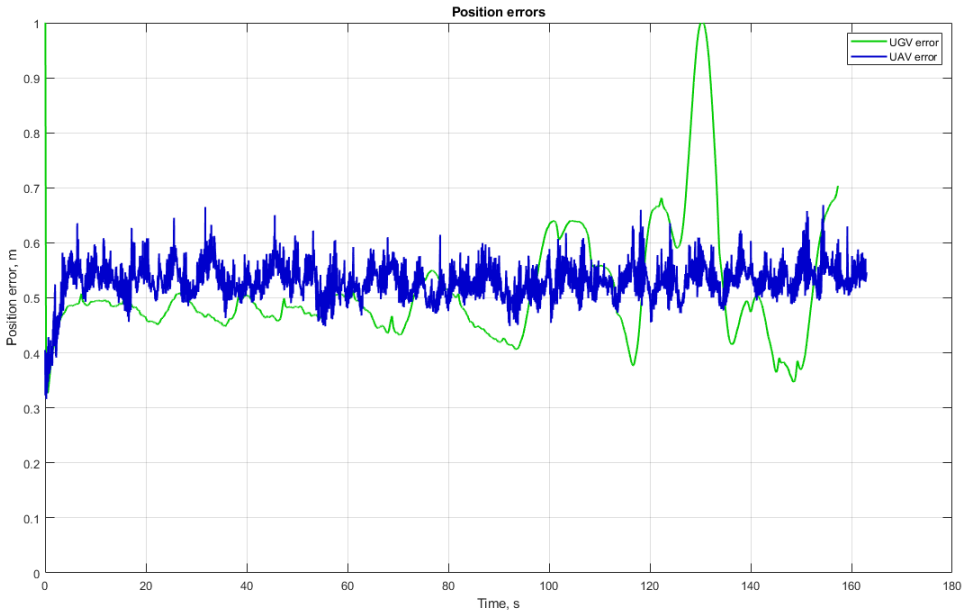

Fig. 7. UGV and UAV coordinates estimation errors without cooperation

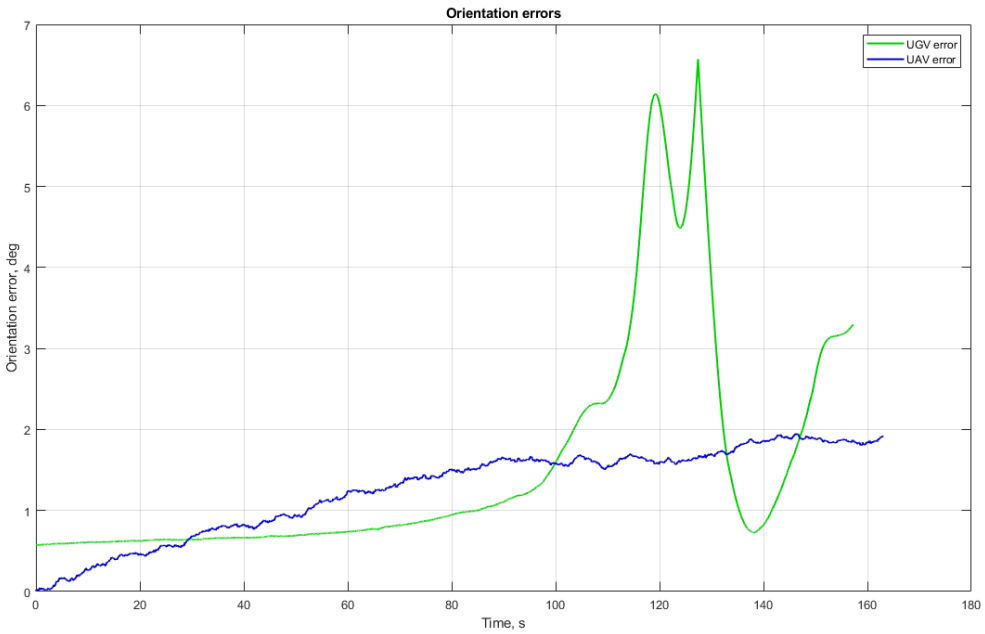

Fig. 8. UGV and UAV orientations estimation errors without cooperation

The resulting position estimation means are 0.51 m and 0.53 m respectively, standard deviations are 0.11 m and 0.03 m. Orientation estimation means are 1.55 deg and 1.26 deg for UGV and UAV respectively with standard deviations: 1.4 deg and 0.54 deg.

Comparing these results with the results presented on fig 3,4 it is clear, that the cooperative navigation approach provides UGV with the accuracy boost of 0.24 m for positioning (considering only the mean values) and 0.79 deg for orientation. For UAV respective accuracy boosts are 0.26 m and 0.86 deg. While the mean error values increase may not seem significant, the positioning accuracy of the UGV has been increased by 47% with cooperative navigation (and 49% for UAV). These results were expected, since cooperative navigation approach integrates additional measurements data into sensor fusion algorithms which convert measurement redundancy into navigation accuracy.

V. Conclusion

In this study, we presented a novel approach to cooperative navigation for ground and aerial robots, leveraging sensor fusion techniques based on the Kalman filter. By enabling these robots to share and integrate their positional information, we achieved significant improvements in navigation accuracy. The simulation results clearly indicate that our proposed method enhances the estimation of each robot's pose relative to its peers, effectively reducing the effects of noise and uncertainty inherent in conventional navigation algorithms.

The collaborative framework not only optimizes the navigation capabilities of both ground and aerial robots but also fosters a more resilient and adaptable system. As the robots work in tandem, they can better navigate complex environments, which is particularly beneficial for a variety of applications such as aircraft inspection, search and rescue missions, environmental monitoring, and logistics.

Future work will focus on experimental testing of the proposed cooperative navigation system. Additionally, the development of the adaptive control algorithms could further enhance the robustness of the navigation strategy. Overall, our findings underscore the potential of cooperative strategies in multi-robot systems, paving the way for more sophisticated autonomous operations in dynamic environments.

Acknowledgments

The research was supported by RSF (project No. 23-29-00958).

References

[1] Zhang, P., Liu, Y., & Du, H. (2024). An integrated framework for UAV-based precision plant protection in complex terrain: the ACHAGA solution for multi-tea fields. *Frontiers in Plant Science*, *15*, 1440234.

[2] Pereira, G. A., Kumar, V., & Campos, M. F. (2004). Decentralized algorithms for multirobot manipulation via caging. *Algorithmic Foundations of Robotics V*, 257-273.

[3] Groenewald, C. A., Saha, G. C., Mann, G., Bhushan, B., Howard, E., & Groenewald, E. S. (2024). Multi-Agent Systems in Robotics: Coordination and Communication using Machine Learning. *NATURALISTA CAMPANO*, *28*(1), 882-897.

[4] Ducatelle, F., Caro, G., Förster, A., Bonani, M., Dorigo, M., Magnenat, S., ... & Gambardella, L. (2014). *Cooperative navigation in robotic swarms. Swarm Intelligence*, *8*, *1-33*.

[5] Salam, T., & Hsieh, M. A. (2023). Heterogeneous robot teams for modeling and prediction of multiscale environmental processes. *Autonomous Robots*, *47*(4), 353-376.

[6] Mugo Moses, H. Robotics in Disaster Response: Enhancing Search and Rescue Operations.

[7] Rajmane, R., Gitay, N., Yadav, A., Patil, Y., & Sonawane, A. (2020). Precision agriculture and robotics. *Int. J. Eng. Res. Tech*, *9*, 17-22.

[8] Aleshin, B. S., Chernomorsky, A. I., Kuris, E. D., Lelkov, K. S., & Ivakin, M. V. (2020). Robotic complex for inspection of the outer surface of the aircraft in its parking lot. *Incas Bulletin*, *12*, 21-31.

[9] Lelkov, K. S., & Chernomorsky, A. I. (2022, May). Integrated Navigation System for Ground Wheeled Robot. In *2022 29th Saint Petersburg International Conference on Integrated Navigation Systems (ICINS)* (pp. 1-4). IEEE.

[10] Chernomorsky, A. I., Lelkov, K. S., & Kuris, E. D. (2020). About One way to increase the accuracy of navigation system for ground wheeled robot used in aircraft parking. *Smart Science*, *8*(4), 219-226.

[11] Savkin, A., Antonov, D., Kolganov, L., Ryabinkin, M., & Chekhov, E. (2021, May). UAV navigation using opto-electronic and inertial means in GNSS-denied environment. In *Journal of Physics: Conference Series* (Vol. 1925, No. 1, p. 012051). IOP Publishing.

[12] Liu, C., Wei, S., Zhang, M., Yan, Q., & Yu, F. (2024). High-Precision Monitoring during the Installation of Large Steel Structures by UAV Nap-of-the-Object Photogrammetry. *The International Archives of the Photogrammetry, Remote Sensing and Spatial Information Sciences*, *48*, 317-323.

[13] Lelkov, K. S. (2023, November). Hex-rotor aircraft dynamics and simulation. In *AIP Conference Proceedings* (Vol. 2948, No. 1). AIP Publishing.

[14] Zharkov, M., Veremeenko, K., Kuznetsov, I., & Pronkin, A. (2022). Experimental results of attitude determination functional algorithms implementation in strapdown inertial navigation system. *Sensors*, *22*(5), 1849.

[15] Veremeenko, K. K., Zharkov, M. V., Kuznetsov, I. M., & Pron'kin, A. N. (2023). Influence of Longitudinal Acceleration Parameters on the Ability of Instrument Error Estimation of Inertial Navigation System. *Russian Aeronautics*, *66*(1), 115-124.
[16] Savkin, A., Antonov, D., Chekhov, E., & Kolganov, L. (2021, May). Method for autonomous navigation based on integrated inertial and opto-electronic measurements. In *2021 28th Saint Petersburg International Conference on Integrated Navigation Systems (ICINS)* (pp. 1-3). IEEE.
[17] Savkin, A., Antonov, D., Chekhov, E., et al. (2023). Method for autonomous navigation based on integrated inertial and opto-electronic measurements. In *Pribory, ISSN 2071-7865, Moscow*, (pp. 19-30). IEEE.
[18] Antonov, D. A., Veremeenko, K. K., Zharkov, M. V., Zimin, R. Y., Kuznetsov, I. M., & Pron'kin, A. N. (2020). Fault-tolerant integrated navigation system for an unmanned apparatus using computer vision. *Journal of Computer and Systems Sciences International*, *59*, 261-275.
[19] Papadakis, P. (2023). *Computer Vision and Robot Navigation in 3D Environments* (Doctoral dissertation, Université de Bretagne Occidentale).
[20] Cai, G., Chen, B. M., Lee, T. H., Cai, G., Chen, B. M., & Lee, T. H. (2011). Coordinate systems and transformations. *Unmanned rotorcraft systems*, 23-34.
[21] Kalman, R. E. (1960). A new approach to linear filtering and prediction problems.
[22] Fatehi, A., & Huang, B. (2017). Kalman filtering approach to multi-rate information fusion in the presence of irregular sampling rate and variable measurement delay. *Journal of Process Control*, *53*, 15-25.
[23] Rajamani, R. (2011). *Vehicle dynamics and control*. Springer Science & Business Media.
[24] Loparev, A. V., Stepanov, O. A., & Chelpanov, I. B. (2012). Using frequency approach to time-variant filtering for processing of navigation information. *Gyroscopy and Navigation*, *3*(1), 9-19.